



# Structure and Reactivity of the Ionic Liquid [C<sub>1</sub>C<sub>1</sub>Im][Tf<sub>2</sub>N] on Cu(111)

Rajan Adhikari<sup>1</sup> · Stephen Massicot<sup>1</sup> · Lukas Fromm<sup>2</sup> · Timo Talwar<sup>1</sup> · Afra Gezmis<sup>1</sup> · Manuel Meusel<sup>1</sup> · Andreas Bayer<sup>1</sup> · Simon Jaekel<sup>1</sup> · Florian Maier<sup>1</sup> · Andreas Görling<sup>2</sup> · Hans-Peter Steinrück<sup>1</sup>

Accepted: 2 March 2023 / Published online: 11 April 2023  
© The Author(s) 2023

## Abstract

We studied the adsorption and reaction behavior of the ionic liquid (IL) 1,3-dimethylimidazolium bis[(trifluoromethyl) sulfonyl]imide ([C<sub>1</sub>C<sub>1</sub>Im][Tf<sub>2</sub>N]) on Cu(111) using non-contact atomic force microscopy (nc-AFM), scanning tunneling microscopy (STM), and angle-resolved X-ray photoelectron spectroscopy (ARXPS) in ultrahigh vacuum as a function of temperature, supported by density-functional theory (DFT) calculations. Our nc-AFM results for sub-monolayer IL films show that at 200 K, the IL self-assembles into highly ordered islands, with cations and anions arranged next to each other in a checkerboard-type phase. After extended annealing at 300 K, the structure transforms first to a hexagonal phase and then to a porous honeycomb phase. Simultaneously, many small, disordered islands are formed. Complementary ARXPS reveals no IL desorption until 300 K. However, a significant fraction of the IL is converted to a new species as deduced from new, strongly shifted peaks that develop in the XP spectra at around 275 K and grow with annealing time at 300 K. We correlate the remaining unshifted peaks to the ordered phases observed in nc-AFM and the shifted peaks to decomposition products, which appear as disordered islands in nc-AFM and STM. Upon further heating to 360 K, about 50% of the anions or their decomposition products desorb from the surface, while cation-related fragments mostly remain on the surface. From DFT, we obtain additional information on the structure of the ordered phases and the interaction of the IL with the substrate.

**Keywords** [C<sub>1</sub>C<sub>1</sub>Im][Tf<sub>2</sub>N] · Ionic liquids · Cu(111) · Non-contact-atomic force microscopy (nc-AFM) · Scanning tunneling microscopy (STM) · Angle-resolved X-ray photoelectron spectroscopy (ARXPS) · Density functional theory (DFT) calculations

## 1 Introduction

Ionic liquids (ILs) are composed of molecular ions and have attracted a lot of attention recently because of their unusual properties, such as a wide temperature range of liquid phase, electrochemical stability, very low vapor pressure at room temperature (RT), good ionic heat capacities, and potential as green solvents [1–5]. These properties render them good candidates for applications in a variety of fields

[2, 6]. Examples are thermal storage [7, 8], electrochemical applications [9], homogeneous catalysis [1, 2, 10, 11], dye sensitized solar cells [12], lubrication [13–15], fuel cell [16], nuclear energy utilization [17], biomedical sphere [18], and even telescope construction [19] to name only the few. Furthermore, by tailoring their properties with different functional groups one obtains task-specific reaction media [4, 20]. Their specific properties are governed by a complex combination of van der Waals, (unscreened) Coulomb, dipole, and hydrogen bonding interactions, which seldom occur together in other materials [21].

ILs are particularly interesting for catalytic applications. Two concepts have been developed and introduced, that is, the supported ionic liquid phase (SILP) approach [10, 22–24] and the solid catalyst with ionic liquid layer (SCILL) approach [24, 25]. In SILP, an IL film containing dissolved transition metal complexes is coated onto a porous support, whereas in SCILL a thin IL film is coated onto the active metal surface of a heterogeneous catalyst [24]. Both

Rajan Adhikari and Stephen Massicot shared first-authorship.

✉ Hans-Peter Steinrück  
hans-peter.steinrueck@fau.de

<sup>1</sup> Lehrstuhl für Physikalische Chemie II, Friedrich–Alexander–Universität Erlangen–Nürnberg, Egerlandstr. 3, 91058 Erlangen, Germany

<sup>2</sup> Lehrstuhl für Theoretische Chemie, Friedrich–Alexander–Universität Erlangen–Nürnberg, Egerlandstr. 3, 91058 Erlangen, Germany

SILP and SCILL systems are already in use commercially [26–28]. For example, Petronas employs a SILP system to capture mercury (Hg) from natural gas [29], while Clariant employs SCILL systems for the selective hydrogenation of unsaturated hydrocarbons [30].

In many applications, the interface of the IL with its environment, that is, IL–support [31, 32] and/or IL–vacuum(gas) interfaces, plays a crucial role [33]. The ultimate design, precise control, and understanding of the structural features of ILs at interfaces open the door to manifold applications in batteries, nanoscale tribology, electrical double-layer capacitors, and other fields. In energy storage devices such as lithium ion batteries, a thorough understanding of ionic behavior at the interface is required to understand the formation of the solid–electrolyte interphase. The noble metals gold, silver and copper are essential materials for such energy storage devices. Cu has been used as a current collector in lithium and sodium ion batteries (see ref [34] and references therein). Thus, understanding the nature of the interaction between an IL and the substrate promises a more controlled design and use of ILs for particular applications. This demand resulted in studies of IL–metal interfaces both *in situ*, under electrochemical conditions [31, 32], and *ex situ*, under ultraclean ultrahigh vacuum (UHV) conditions [35, 36]. Detailed information on the IL/substrate interface, obtained mostly by angle resolved X-ray photoelectron spectroscopy (ARXPS) and scanning tunneling microscopy (STM) on well-defined single crystal surfaces in UHV, can be found in a review article by Lexow et al. (see Ref. [36] and references therein), and in a number of earlier reviews, which also include data from ultraviolet photoelectron spectroscopy (UPS), inverse photoelectron spectroscopy (IPES), in addition to ARXPS (see Refs. [11, 35, 37–39] and references therein).

Most of the studies by ARXPS and/or STM have been done on inert single crystal surfaces such as Au(111) or Ag(111) [36, 40–42]. In nearly all cases, the formation of a wetting layer was observed, with both anions and cations adsorbed in a checkerboard-like structure in direct contact to the surface. This structure was initially derived from ARXPS, but was later on confirmed by molecularly resolved STM measurements at temperatures well below room temperature. The detailed structure and also stable imaging temperature thereby depended on the particular IL and the substrate. Quite recently, the experimental methods were complemented by non-contact atomic force microscopy (nc-AFM). Meusel et al. demonstrated for  $[C_1C_1Im][Tf_2N]$  on Au(111) that with variable temperature nc-AFM highly ordered structures can even be resolved at room temperature and above [43, 44]. At low temperature, they observed the coexistence of a stripe phase and a hexagonal phase—with

single molecule thickness—for the first layer on the surface. In this previous study, the individual anions in the wetting layer were identified from their larger height as compared to the flat-lying (and thus invisible) cations [43]. A stripe phase was also resolved for coverages in the multilayer range, where the growth proceeds through bilayer formation, demonstrating the layer-by-layer 2D growth of this IL on the very inert Au(111) surface [44]. Moreover, for certain substrate temperatures, upon deposition metastable 3D droplets were initially formed on top of the wetting layer, which converted into the 2D bilayer structure over time [45].

The aim of this study was to move on to the more reactive Cu(111) surface and investigate the adsorption, thermal evolution and possible reactions of  $[C_1C_1Im][Tf_2N]$  on this surface in order to determine potential differences to the Au(111) surface. This topic also appeared quite interesting to us, since in literature there are two studies for related systems, that is, by Biedron et al. for  $[C_8C_1Im][Tf_2N]$  on Cu(100) [46] and by Uhl et al. for  $[BMP][Tf_2N]$  on Cu(111) [47]. Interestingly, the results seemed to be in conflict with each other, but based on our study a reinterpretation of the data on Cu(111) leads to a consistent picture. We performed our study using *in situ* ARXPS (100–800 K) and variable temperature nc-AFM/STM (100–350 K). The scheme at the top of Table 1 shows the chemical and molecular structure of  $[C_1C_1Im][Tf_2N]$ . The nc-AFM/STM studies with sub-molecular resolution were performed for coverages around 0.15 monolayer (ML) of ion pairs, which corresponds to 30% of a full wetting layer (=0.30 WL) of  $[C_1C_1Im][Tf_2N]$  on Cu(111). To obtain complementary information, ARXPS measurements were performed for 0.3 and 0.5 ML. In addition, DFT calculations provide complementary insight into the structure and the bonding situation of the IL adlayer. To the best of our knowledge, this is the first time that individual ion pairs have been resolved and identified in an IL adlayer on Cu(111) using nc-AFM.

## 2 Experimental

The ionic liquid  $[C_1C_1Im][Tf_2N]$  was either bought from IoLiTec (used in the XPS measurements) or synthesized under ultra-clean conditions described in a previous publication [48] (used in the nc-AFM/STM measurements). It was thoroughly degassed under ultrahigh vacuum (UHV) prior to deposition to remove volatile impurities. In the literature, the cation  $[C_1C_1Im]^+$  is also known as  $[MMIm]^+$  [49], and the anion  $[Tf_2N]^-$  as  $[NTf_2]^-$  [50] or  $[TfSA]^-$  [51]. The scanning probe microscopy (SPM) and the ARXPS experiments were performed in two separate UHV systems. In both, the

**Table 1** Different structures and the corresponding unit cell parameters and unit cell areas, as obtained from nc-AFM and STM

Structure	Unit cell parameters	Matrix notation	Unit cell area [nm <sup>2</sup> ]	Ion pair density ( $\rho$ ) [ion pairs/nm <sup>2</sup> ]
Checkerboard-type (nc-AFM)	$ \vec{a} =1.90\pm 0.08$ nm $ \vec{b} =0.90\pm 0.05$ nm $\gamma=90\pm 3^\circ$	$\begin{bmatrix} 6 & 2 \\ -3 & 4 \end{bmatrix}$ $\gamma=92.2^\circ$	1.71	1.17
Hexagonal-type (nc-AFM)	$ \vec{a} = \vec{b} =2.35\pm 0.08$ nm $\gamma=60\pm 4^\circ$	$\begin{bmatrix} 8 & 2 \\ -2 & 10 \end{bmatrix}$ $\gamma=60^\circ$	4.78	1.26
Honeycomb-type (nc-AFM)	$ \vec{a} = \vec{b} =2.35\pm 0.08$ nm $\gamma=60\pm 4^\circ$ pore diameter ~ 2 nm	$\begin{bmatrix} 8 & 2 \\ -2 & 10 \end{bmatrix}$	4.78	1.05
Honeycomb-type (STM)	$ \vec{a} = \vec{b} =2.36\pm 0.08$ nm $\gamma=60\pm 4^\circ$ pore diameter ~ 2 nm	$\gamma=60^\circ$	4.82	1.04

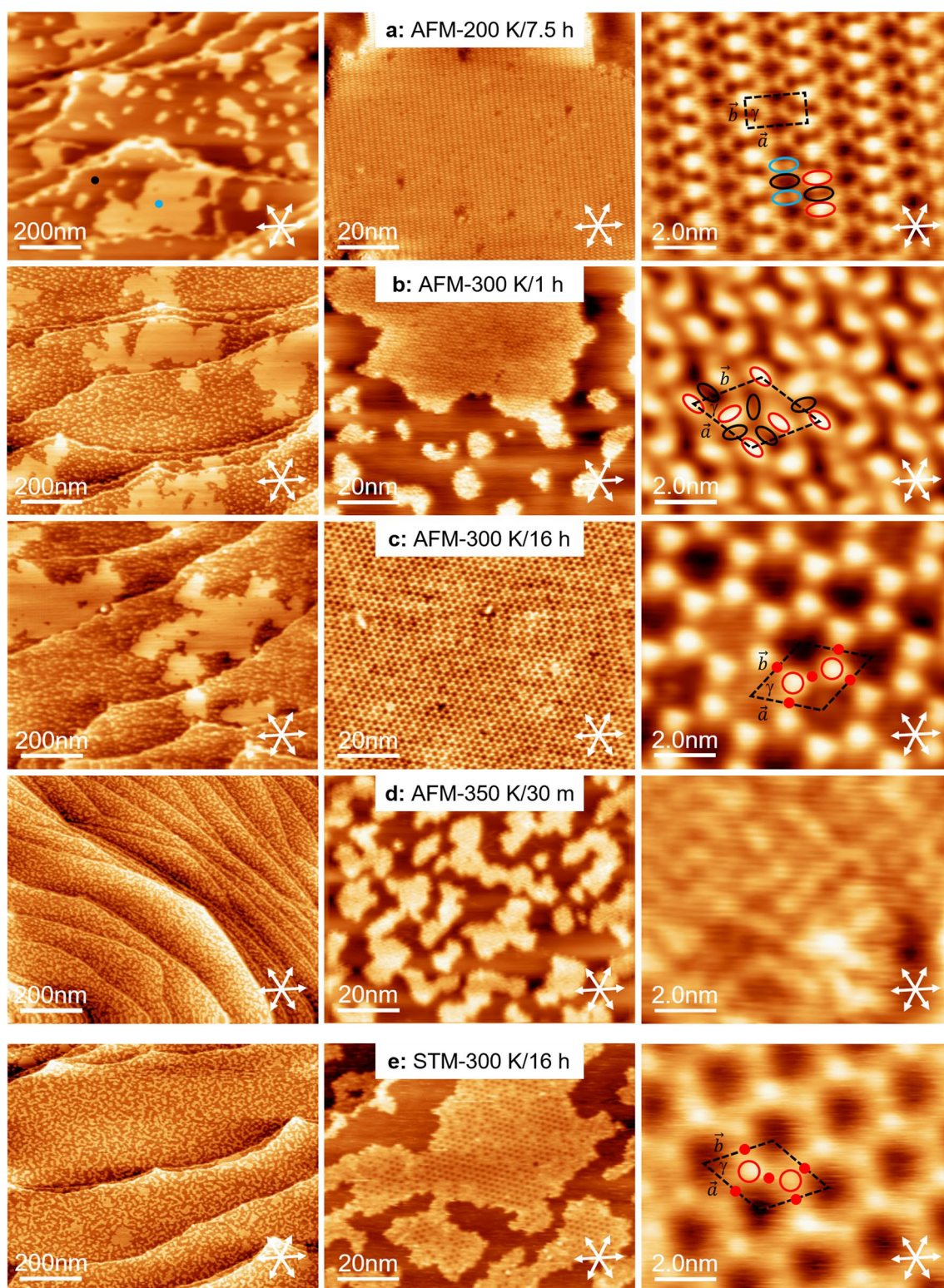
Also given are the unit cell area and the ion pair density,  $\rho$ ; for details see text. On top of the table the chemical and molecular structure of [C<sub>1</sub>C<sub>1</sub>Im][Tf<sub>2</sub>N] is depicted together with height of the cation (~0.3 nm) and anion (~0.5 nm); grey: C, white: H, blue: N, red: O, yellow: S, and green: F

clean Cu(111) surface was freshly prepared prior to each IL deposition using sequential cycles of Ar<sup>+</sup> ions bombardment (0.6 to 1 keV) at room temperature followed by a final annealing step at 800 to 900 K for approximately 10 min and consecutive cooling to the desired temperatures. The IL was deposited by physical vapor deposition (PVD) onto the substrate held at different temperatures as denoted using a home-built Knudsen cell [52] with the crucible temperature of 385–398 K. To ensure stable and reproducible evaporation rates, the IL adsorbate flux was monitored with a quartz crystal microbalance (QCM). IL coverages are denoted in ML, where 1 ML corresponds to a complete layer of vertically rented ion pairs. In case of a checkerboard structure with anions and cations adsorbed next to each other in direct contact to the surface, this coverage corresponds to 0.5 ML, which is also denoted as 1 WL (wetting layer).

The variable temperature nc-AFM and STM measurements were carried out in a two-chamber UHV system, using a Scienta Omicron VT-AFM-Q + -XA microscope, with a base pressure in the low 10<sup>-11</sup> mbar range [43]. Following IL deposition on the sample in the preparation chamber, it was then quickly transferred to the pre-cooled AFM/STM sample stage in the analysis chamber at 110 K for the measurements. All AFM images were obtained in non-contact mode with

silicon cantilevers, and the applied frequency shifts  $\Delta f$  in the employed experimental conditions ranged from – 300 to – 650 Hz vs the cantilever's resonance frequency, which is typically around ~ 270 to 300 kHz. The STM images were obtained with a manually cut Pt/Ir tip in constant current mode. The denoted bias voltages refer to voltages applied to the tip relative to the sample potential. The nc-AFM/STM images were processed using the WSxM software [53]. For noise reduction, moderate filtering (background subtraction, Gaussian smoothing) was applied.

The ARXPS measurements were performed in a two-chamber XPS system, which has previously been described in detail elsewhere [54]. The XP spectra were obtained using a non-monochromated Al K $\alpha$  X-ray source (SPECS XR 50, 1486.6 eV, 240 W) and a hemispherical electron analyzer (VG SCIENTA R3000). For all spectra, a pass energy of 100 eV was used, yielding an overall energy resolution of 0.9 eV [54]. The spectra were quantitatively evaluated using CasaXPS V2.3.16Dev6. For the Cu 2p<sub>3/2</sub> and the Auger-LMM substrate signals, Shirley backgrounds were subtracted and peaks were fitted with Lorentzian line shapes. For the IL-related S 2p, C 1s, N 1s, O 1s and F 1s regions, the positions and widths (fwhm) of the peaks were constrained (see Table S2 in the SI).



### 3 Theory

First-principles DFT calculations were performed with the VASP program package (Version 5.4.1) [55–57] using the PBE exchange–correlation functional [58]. The projector

augmented wave method (PAW) [59] was used to take into account the core electrons. An energy cutoff of 450 eV was chosen for the plane wave basis. To describe the long-ranged London dispersion interactions the DFT-D3 correction scheme [60] was applied, and a Methfessel-Paxton smearing

**Fig. 1** nc-AFM (a–d) and STM images (e) of 0.15 ML  $[C_1C_1Im][Tf_2N]$  on Cu(111), as overview (left,  $1000 \times 800 \text{ nm}^2$ ), close-up (middle,  $100 \times 80 \text{ nm}^2$ ), and with high resolution (right,  $10 \times 8 \text{ nm}^2$ ). **a** After annealing at 200 K for 7.5 h, ordered islands with a checkerboard-type structure and a nearly rectangular unit cell are observed; the right image is an average frame of nine consecutively recorded images. **b** After annealing at 300 K for 1 h, disordered small islands coexist with large ordered islands with hexagonal structure. **c** After annealing at 300 K for ~16 h, disordered small islands coexist with large IL islands with a highly ordered porous honeycomb structure. **d** After annealing at 350 K for 30 min, only small disordered islands are found. **e** STM images following a different preparation route and annealing at 300 K for ~16 h (see text) display the same honeycomb structure as seen in (c). The nc-AFM images were measured with  $\Delta f = -400$  or  $-500$  Hz, and the STM images with  $U_{bias} = 2$  V and  $I_{set}$  of 0.2 or 0.4 nA (for details, see Table S4 in the SI); the unit cells are shown as dashed black lines; covered and uncovered areas are denoted by blue and black dots, respectively. For more details see text

[61] with a broadening of 0.2 eV was included. A supercell approach with four layers of Cu atoms was used to model the systems, including a 20 Å layer of vacuum separating periodic images in  $z$ -direction. The experimental lattice parameter of 3.58 Å was used for the Cu bulk geometry. The two bottom layers were fixed, while the top two layers were relaxed during the optimizations. The geometry was optimized until all forces were smaller than 0.01 eV/Å. The model for the checkerboard structure with a  $\begin{bmatrix} 6 & 2 \\ -3 & 4 \end{bmatrix}$  supercell was calculated with a  $2 \times 4 \times 1$  and the larger hexagonal structures with the  $\begin{bmatrix} 8 & 2 \\ -2 & 10 \end{bmatrix}$  supercell with a  $2 \times 2 \times 1$  Gamma centered Monkhorst–Pack [62]  $k$ -point mesh. Adsorption energies  $E_{ads}$  were calculated as total energy differences between the clean surface unit cell  $E_{surf}$  plus the energy of the ions in gas phase  $E_{an} + E_{cat}$  minus the total energy of the combined system  $E_{sys}$  as  $E_{ads} = E_{an} + E_{cat} + E_{surf} - E_{sys}$ . Therefore, higher adsorption energies correspond to higher stability. The reference of the ionic liquid are the isolated ions in gas phase and not in the liquid phase. Isolated ions in gas phase represent the most simple and best defined reference. Furthermore, the comparison of different adsorption structures is not affected by the choice of the reference.

## 4 Results and Discussion

### 4.1 Atomic Force Microscopy and Scanning Tunneling Microscopy

In a first step, we investigated the adsorption and reaction behavior of 0.15 ML (=0.30 WL) of  $[C_1C_1Im][Tf_2N]$  on Cu(111) using nc-AFM. The layers were deposited with the sample at 300 K. After deposition, the sample was immediately transferred to the precooled nc-AFM stage at 110 K

within 7 to 10 min, in order to avoid the progress of potential chemical reactions (as it will be shown later, changes at 300 K only occur very slowly over several hours). Thereafter, nc-AFM images were first measured at 110 K, and then the sample was stepwise-annealed for extended times to 200, 250, 300 and 350 K. After each annealing step, the sample was quickly cooled back to 110 K to freeze the present state for imaging.

Figure 1a shows the corresponding images after annealing to 200 K for 7 h 30 min. In the overview image (left), we observe extended IL islands of various sizes (left image, bright areas) at the steps and also on the terraces of the Cu(111) surface; IL-covered areas and large areas of uncovered Cu substrate are indicated by blue and black dots, respectively. Notably, directly after cooling to 110 K, very similar structures are observed, but with a smaller size of the ordered islands and reduced resolution (see SI, Figure S1). The IL islands are observed close to step edges from both the ascending and descending sides of the step edges, implying that the steps are energetically favored adsorption sites that serve as nucleation centers. The close-up in Fig. 1a (middle) shows one representative large island connected to a step edge. This island consists of a highly regular, close-packed phase with only few defects, giving rise to a stripe-like appearance. The high-resolution AFM image of one of the islands in Fig. 1a (right) reveals that the close-packed phase is characterized by molecular rows, that is, stripes with a nearly rectangular unit cell ( $\gamma = 90 \pm 3^\circ$ ), with lattice vectors  $\vec{a}$  ( $1.90 \pm 0.08 \text{ nm}$ ) and  $\vec{b}$  ( $0.90 \pm 0.05 \text{ nm}$ ), and a unit cell area  $1.71 \text{ nm}^2$  (see Table 1). From the measured angle of  $6^\circ$  between the unit cell vector  $\vec{a}$  and the substrate high symmetry direction, we derive a commensurate  $\begin{bmatrix} 6 & 2 \\ -3 & 4 \end{bmatrix}$  superstructure, using standard matrix notation with a unit cell angle of  $92.2^\circ$ . We propose that the unit cell contains 2 ion pairs, yielding a density of  $1.17 \text{ ion pairs/nm}^2$ . This analysis is based on the comparison to the low-temperature checkerboard-type structures on Au(111), with one ion pair per unit cell, and unit cell areas between  $0.74$  and  $0.85 \text{ nm}^2$  [43]. We assign the very bright oval protrusion (red ellipses) and the two less bright protrusions (blue ellipses) to two differently oriented anions, and the dark areas in between (black ellipses) to the two cations; for more details, see DFT results below. From this consideration, we conclude that the anion to cation ratio is 1:1, that is, the ion pairs on the Cu(111) surface remain intact and are arranged in a checkerboard-type ionic surface tiling without dissociation, self-assembling into stripes. We will address the details of the structure together with the DFT calculations presented later on.

In a next step, we annealed the deposited layer at 250 K and then at 300 K. After annealing to 250 K for 45 min, we again find images with a stripe structure, albeit with a lower

resolution of the image (see SI, Figure S2), which likely is due to a different termination of the AFM tip.

After annealing to 300 K for 1 h, we observe a pronounced transformation of the film structure, which is evident from the corresponding nc-AFM images in Fig. 1b. In the overview image (left), large islands are found to coexist with many small islands distributed all over the surface (see also Figure S3 in the SI). The close-up image (middle) reveals long-range order for the large islands, and disorder for the small islands. In the high-resolution nc-AFM image of one of the large islands in Fig. 1b (right), we observe a hexagonal-type lattice with three bright longish protrusions (red ellipses) and three less bright protrusions (black ellipses) per unit cell (dashed black rhombus); the protrusions in the unit cell have different orientation. The unit cell lattice vectors  $\vec{a}$  and  $\vec{b}$  both have a length of  $2.35 \pm 0.08$  nm with  $\gamma = 60 \pm 4^\circ$ , resulting in a unit cell area of  $4.78$  nm<sup>2</sup>. Assuming that each protrusion now represents an ion pair (see thorough discussion below), we obtain six ion pairs per unit cell. The resulting density of  $1.26$  ion pairs/nm<sup>2</sup> is quite comparable to that of the stripe phase (see Table 1). The absence of long range order for the small islands is also evident from the high-resolution image shown in Figure S4 (left) in the SI.

After extended annealing to 300 K for 16 h, we see another pronounced change in the structural order of the adsorbed IL layer; see Fig. 1c. In the overview nc-AFM image (left) we again find large islands coexisting with a large number of small islands; the close-up image (middle) shows a highly ordered honeycomb structure of the large islands, while the small islands are again disordered (see also Figure S4 (middle) in the SI). From the high-resolution nc-AFM image of one of the large islands in Fig. 1c (right), we conclude that the unit cell (dashed black rhombus) contains two bright protrusions (red circles) and three less bright protrusions (red dots); we again assume that each protrusion corresponds to one ion pair. The lengths of the lattice vectors  $\vec{a}$  and  $\vec{b}$  are again  $2.35 \pm 0.08$  nm with  $\gamma = 60 \pm 4^\circ$ , resulting in a unit cell area of  $\sim 4.78$  nm<sup>2</sup>. Assuming five ion pairs per unit cell (see below), we obtain a density of  $1.05$  ion pairs/nm<sup>2</sup> (see Table 1). From the angle of  $12^\circ$  between the unit cell vectors and the substrate high symmetry directions we derive a  $\begin{bmatrix} 8 & 2 \\ -2 & 10 \end{bmatrix}$  superstructure using standard matrix notation, with an angle of  $60^\circ$ , for the porous honeycomb mesh. The pores of the honeycomb mesh have a diameter of roughly 2 nm. Interestingly, the size of the unit cell of the honeycomb structure is identical to that of the hexagonal structure (that is, lattice vector lengths of 2.35 nm), within the experimental uncertainty. Note that the honeycomb structure can be obtained from the overall hexagonal structure by removing one bright protrusion (that is, one ion pair), which results in the pore of the honeycomb structure. Thus,

the hexagonal structure can be seen as transition structure from the stripe phase to the honeycomb phase upon annealing the IL layer at 300 K.

Upon further heating to 350 K, the long-range ordered islands disappear, and only small, disordered islands are observed; see Fig. 1d, which is particularly evident from the high-resolution image (right). Interestingly, the appearance of these small islands is very similar to that of the above described small, disordered islands, which coexist with the hexagonal and honeycomb structures at 300 K (see comparison in Figure S4 in the SI).

Notably, we also obtain the honeycomb structure following a different preparation and measurement route. In contrast to the above-described preparation where the IL was deposited at room temperature and quickly cooled down to 110 K, we here deposited 0.15 ML (=0.30 WL) of [C<sub>1</sub>C<sub>1</sub>Im][Tf<sub>2</sub>N] onto Cu(111) held at low temperature ( $T < 160$  K), and measured at 110 K; here, the measurements were performed by STM and not by nc-AFM. While after adsorption at  $< 160$  K and also after annealing up to 250 K (for 15 min) no ordered IL islands could be found (see Figure S5 in SI), ordering is observed starting after extended annealing for 3–16 h at 300 K. The corresponding STM images after annealing for 16 h are shown in Fig. 1e. The overview image (left) shows the surface homogeneously covered with many small islands. When comparing these STM images with the previous nc-AFM overview images obtained after deposition at 300 K followed by immediate cooling to 110 K and then annealing to 300 K (Fig. 1c), we see much larger islands for the latter, which is attributed to Ostwald ripening during deposition at 300 K. After annealing the  $< 160$  K-deposited layer for 3–16 h at 300 K, we observe again two distinctly different structures coexisting on the surface: The close-up STM image in Fig. 1e (middle) shows a large IL island with a well-ordered inner part surrounded by a disordered rim; in addition, smaller disordered separate islands are seen. The well-ordered inner part of the large island displays the porous honeycomb structure with few defects and additional species in some pores, as deduced from their less-dark appearance. Figure 1e (right) shows the high-resolution STM image of the center of the island, with the primitive unit cell indicated by the dashed black rhombus. The porous honeycomb-type adlayer again has a primitive hexagonal unit cell. The lattice vectors  $\vec{a}$  and  $\vec{b}$  have an identical length of  $2.36 \pm 0.08$  nm with  $\gamma = 60 \pm 4^\circ$ , resulting in a pore diameter of  $\sim 2$  nm. The unit cell (area of  $4.82$  nm<sup>2</sup>) again contains two bright (red circles) and 3 less bright (red dots) protrusions, giving a density of  $1.04$  ion pairs/nm<sup>2</sup>; these parameters are identical to those observed using the other preparation route and nc-AFM as imaging technique. The comparison of the close-up images (middle) and high resolution images (right) for the two preparation routes in

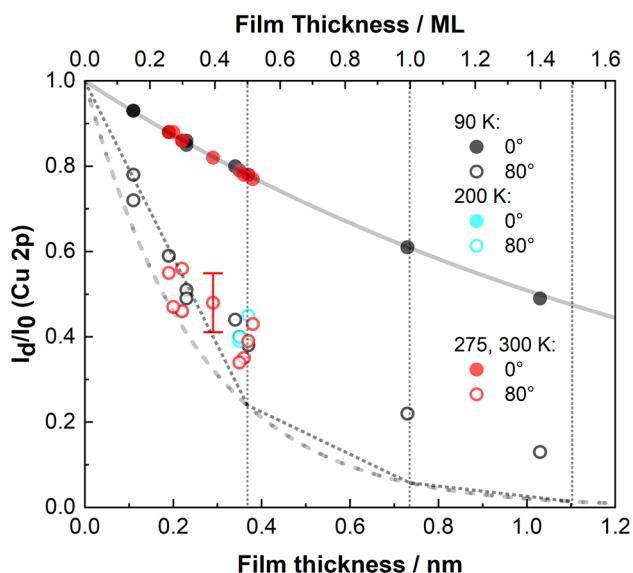


**Fig. 2** Dependence of the Cu 2p substrate signal (full symbols for 0° and open symbols for 80° emission) on IL film thickness for  $[C_1C_1Im][Tf_2N]$  on Cu(111) at 90, 200, 275 and 300 K. The film thickness of each layer was calculated from the attenuation of the Cu 2p signal at 0°. The solid and long-dashed lines show the exponential decay expected for a uniform increase in layer thickness for emission angles of 0° and 80°, respectively [36], based on the inelastic mean free path  $\lambda$  of 3.0 nm for the Cu 2p peak; the short-dashed lines for 80° are the prediction for perfect 2D layer-by-layer growth (section-wise filling of one layer of flat lying ion pairs after another, each with 0.5 ML coverage, see vertical lines). Up to 0.3 ML, very good agreement of the 80° data with the short-dashed lines is found, indicating the formation of a 2D layer; the fact that between 0.3 and 0.5 ML somewhat larger values are found indicate a small deviation from perfect 2D growth. For larger coverages, pronounced deviations from 2D growth are observed

Fig. 1 reveals a higher degree of order and less defects for the deposition at 300 K followed by fast cooling to 110 K.

## 4.2 X-ray Photoelectron Spectroscopy

### 4.2.1 Growth Behavior

Complementing the local scanning probe microscopy data, we also used XPS to follow the overall IL film growth. Figure 2 shows the attenuation of the normalized Cu  $2p_{3/2}$  signal  $I_d/I_0$  upon deposition of  $[C_1C_1Im][Tf_2N]$  at 90, 200, 275 or 300 K. After each deposition step, we measured the signals at both 0° and 80° emission angle. Under the assumption of perfect 2D growth, one can use the attenuation of the Cu 2p substrate signal at 0°,  $I_d/I_0$ , to calculate the mean film thickness  $d$  of the IL layer. From this thickness, we can then predict the attenuation at 80° for a two-dimensional IL layer at this thickness: the short-dashed grey lines represent ideal layer-by-layer 2D growth behavior in 80° for the WL (0.5 ML thickness) and another two layers on top

(the long-dashed grey line represents exponential decay and agrees with the short dashed lines for each completed layer, e.g. at 0.5 ML; for details of this approach, see refs [36, 63]. A coincidence of the measured 80° data with the predicted short-dashed lines reveals perfect 2D growth; 80° data falling above the lines indicate a deviation from layer-by-layer growth towards island growth (3D growth). Focusing first on low coverages/thicknesses up to 0.5 ML, the 80° data (open symbols) in Fig. 2 fall on or close to the short-dashed line until 0.3 ML, independent of temperature, indicating perfect 2D growth in this coverage regime. Interestingly, between 0.3 and 0.5 ML, all measured data systematically are slightly above the calculated 80° curve, which is attributed to moderate 3D growth. Such a behavior is rather unusual, since 2D growth of the first wetting layer up to 0.5 ML has been observed for a wide variety of ILs on different metal surfaces, independent of the growth mode at higher coverages. Examples are  $[C_1C_1Im][Tf_2N]$  on Au(111) [64] and Ag(111) [63],  $[C_8C_1Im][Tf_2N]$  on Ag(111) [63] and Au(111) [64] or  $[BMP][Tf_2N]$  on Au(111) [41]. The formation of the first flat wetting layer is commonly attributed to strong attractions of the ions towards the metal, e.g. by image dipoles. Above 0.5 ML, the 80° data Fig. 2 fall well above the dashed curve for ideal 2D-growth. This deviation is attributed to island formation in the multilayer regime. Note that such Stranski–Krastanov-type growth behavior is quite commonly observed for ILs with short chains, e.g. for  $[C_1C_1Im][Tf_2N]$  on Ag(111) [63] or  $[C_2C_1Im][TfO]$  on Au(111) [36, 65].

### 4.2.2 Adsorption and Thermal Evolution

In order to understand the ongoing surface chemistry of the IL in contact with the Cu(111) surface, we studied the IL layer in the low-coverage regime, during deposition and annealing by XPS. We performed measurements of all relevant IL core levels at selected temperatures, which are characteristic for the changes observed in nc-AFM, that is, 200, 275, 300 and 360 K. We investigated two coverages, namely 0.3 ML and 0.5 ML, which correspond to a partly (0.6 WL) and a more or less fully closed (1.0 WL) wetting layer, respectively; smaller coverages could not be studied reliably, due to poor signal intensities. Nevertheless, the measurements should allow for a comparison to the nc-AFM/STM measurements, which were performed for a 0.15 ML (=0.30 WL) coverage. XP spectra were measured for all core levels at 0° emission angle (and additionally at 80° for 200 K). The corresponding S 2p, C 1s, N 1s, O 1s and F 1s spectra are shown in Fig. 3 (0.5 ML) and Figure S6 (0.3 ML), along with their fits. Data at 0° and 80° are plotted in grey and blue, respectively. In addition, we also measured the corresponding 0° spectra of a multilayer film of 4.6 ML  $[C_1C_1Im][Tf_2N]$ , deposited at 90 K, as reference; these spectra are also included in Figs. 3 and S6 (bottom),

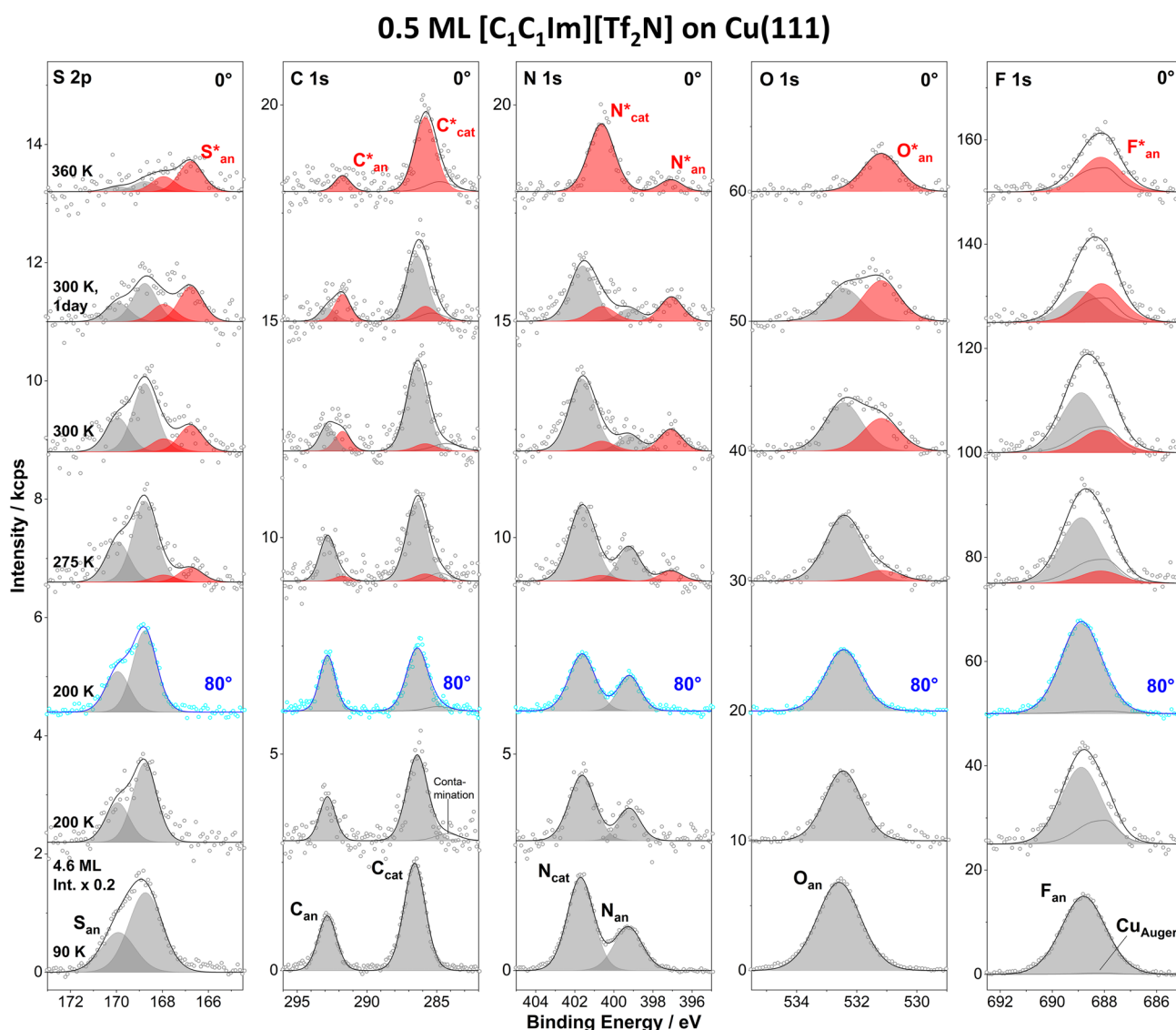


**Fig. 3** S 2p, C 1s, N 1s, O 1s and F 1s spectra of 0.5 ML [C<sub>1</sub>C<sub>1</sub>Im][Tf<sub>2</sub>N] on Cu(111) from 200 to 360 K, along with the spectra for 4.6 ML obtained at 90 K as reference for the bulk IL (bottom). For each denoted temperature, a new layer was freshly prepared and measured under normal (0°) and grazing emission (80°; shown only for 200 K in blue). For a better visualization, the 4.6 ML spectra are scaled

down by a factor of 0.2. Grey peaks indicate the signals of the intact IL, red peaks denote the peaks of the new species formed upon heating. In the C 1s spectra a small contamination of the surface was taken into account, as indicated exemplarily in the spectrum at 200 K; in the F 1s spectra, the overlapping Cu<sub>Auger</sub> signal was subtracted (for more details, see experimental section and SI)

downscaled by the factor 0.2 for better visualization. The quantitative analysis of the 0.5 ML spectra is provided in Table 2, and that of the 0.3 ML spectra in Table S1.

We start with discussing the 0° spectra of the 4.6 ML multilayer film at 90 K, as it represents the unperturbed intact IL. The cation displays two distinct peaks in the N 1s and C 1s region. The C<sub>cat</sub> peak at a binding energy of 286.6 eV is assigned to the three carbon atoms of the imidazolium ring and the two carbon atoms of the methyl groups attached to the nitrogen atoms. The N<sub>cat</sub> peak at 401.7 eV corresponds to the two nitrogen atoms in the imidazolium

ring. For the [Tf<sub>2</sub>N]<sup>-</sup> anion, the C<sub>an</sub> peak at 292.8 eV and the F<sub>an</sub> peak at 688.8 eV are assigned to the carbon and the fluorine atoms of the CF<sub>3</sub> group. The O<sub>an</sub> peak at 532.6 eV and the S<sub>an</sub> 2p<sub>1/2</sub> and 2p<sub>3/2</sub> duplet at 169.9 and 168.7 eV originate from the oxygen and sulphur of the sulfonyl-group, respectively, and the N<sub>an</sub> peak at 399.3 eV stems from the imidic nitrogen. The composition of the 4.6 ML film in Table 2 is in good agreement with the nominal composition within the experimental uncertainty (± 10%), confirming that the IL stays intact in the deposition process, in line with earlier studies [36].



**Table 2** Quantitative analysis of the composition of 0.5 ML  $[C_1C_1Im][Tf_2N]$  on Cu(111) at different temperatures, as derived from the XP spectra shown in Fig. 3 at 0° (and for 200 K also at 80°) emission angle

Temperature	$S_{an, sum}$	$C_{an, sum}$	$C_{cat, sum}$	$N_{cat, sum}$	$N_{an, sum}$	$O_{an, sum}$	$F_{an, sum}$	$\Sigma$
Nominal	<b>2</b>	<b>2</b>	<b>5</b>	<b>2</b>	<b>1</b>	<b>4</b>	<b>6</b>	<b>22</b>
360 K	0.9	0.7	4.1	1.9	0.3	2.0	3.5	13.3
300 K, 1 day	1.6	1.7	4.6	2.0	0.9	4.0	7.1	22.0
300 K	1.8	1.6	4.6	2.1	0.8	3.8	7.3	22.0
275 K	1.9	1.9	4.7	2.1	1.0	3.5	7.0	22.0
200 K, 80°	1.7	2.3	3.4	1.6	0.9	3.2	8.9	22.0
200 K	1.7	1.8	4.7	1.8	0.8	3.6	7.5	22.0
90 K	1.8	2.0	4.6	2.0	1.0	4.2	6.4	22.0

Bold value are nominal numbers, non-bold values are experimental data

Also given are the results for 4.6 ML deposited at 90 K and measured under 0° emission as reference for the bulk IL. For quantification, the shifted (marked with asterisk) and the unshifted signals of the IL were combined to provide the total atom number for each element

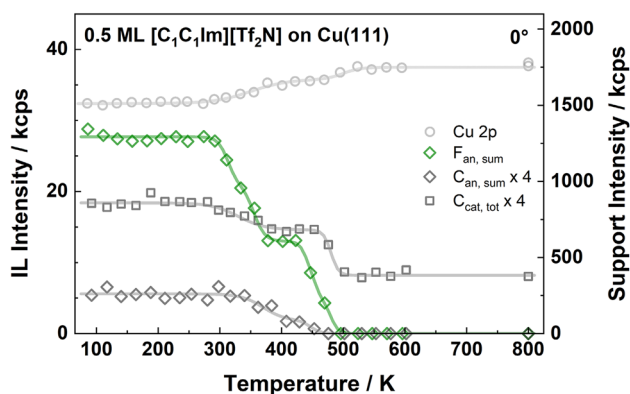


**Fig. 4** Thermal evolution of the Cu 2p (open light grey circles), F 1s (green diamonds) and C 1s (dark grey squares for  $C_{an}$ , and dark grey diamonds for  $C_{het,comb}$ ) intensities during heating a 0.5 ML  $[C_1C_1Im][Tf_2N]$  film on Cu(111). The IL was first deposited onto the sample at 88 K via PVD; thereafter, XP spectra were recorded while heating with a linear heating rate of 2 K/min up to 600 K; after flashing the sample eventually to 800 K for 5 min, a last data set was also recorded. The intensity scale for the Cu 2p signal is given on the right side and that of the F 1s and C 1s signals on the left. The symbols for the corresponding F and C species represent the sums of the corresponding unshifted and shifted (\*) intensities; note that in case of the  $C_{cation}$  region, only one broad peak could be used including the minor carbon contamination (see also Fig. 3 and for further details, see text)

The spectra for 0.5 and 0.3 ML  $[C_1C_1Im][Tf_2N]$  were recorded for all IL core levels at temperatures, at which we expected characteristic changes based on the thermal evolution observed in Fig. 1 and also Fig. 4 (see below); the full data set required ~90/130 min for all core levels of the 0.5/0.3 ML films. To minimize the influence of beam damage, always a new film was freshly prepared and measured at the indicated temperatures of 200, 275 and 300 K, except for the 360 and 500 K films, which were deposited at 300 and 200 K, respectively. Since the behavior is quite similar, the data for 0.5 and 0.3 ML will be discussed together. Thereby, the focus will be on the 0.5 ML films,

since the 0.3 ML films are more prone to beam damage, due to the longer measurement times required for the lower coverage.

For 200 K, we address the spectra at 0° (normal emission) and at 80° (grazing emission) in Fig. 3 (0.5 ML) and Figure S6 (0.3 ML), which allow for deriving information on the stoichiometry as well as the orientation of the IL on the surface. The 0° spectra are, apart from their lower intensities, very similar to those of the multilayer. The only difference is a small shift of some levels by up to 0.2 eV to lower binding energy, yielding the cation peaks  $C_{cat}$  at 286.4 eV and  $N_{cat}$  at 401.6 eV, and the anion peaks  $C_{an}$  at 292.8 eV,  $F_{an}$  at 688.9 eV,  $O_{an}$  at 532.4 eV,  $N_{an}$  at 399.2 eV, and the  $S_{an}$  duplet at 170.0/168.8 eV (for 0.5 ML); for an overview of the binding energies see Table S2 in the SI. These small shifts are attributed to more efficient screening due to the proximity of the metal surface (final state effect). For the analysis of the F 1 s region, the  $Cu_{LMM}$  Auger peak at 688.0 eV, which overlaps with the  $F_{an}$  signal of the anion, has to be considered. This is done by using the Auger peak shape of the clean copper surface, downscaling it according to the IL-film related attenuation of the Cu 2p signal. By fitting the F 1 s peak taking into account this downscaled Auger peak, we obtain the correct number of F atoms in Table 2 (note that at elevated temperatures, new species with shifted binding energies appear as discussed below; in Table 2, only the sum for each atom is given). The quantitative analysis of the 0° spectra in Table 2 (0.5 ML) and Table S1 (0.3 ML) yields atom numbers close to the nominal values within the experimental uncertainty ( $\pm 10\%$ ); the somewhat too large value of the F 1 s signal is attributed to uncertainties in the described Auger peak correction procedure. The very good agreement of XPS quantification in 0° and IL stoichiometry again is a clear indication that the IL adsorbs intact at 200 K.

From the quantitative analysis of the 80° spectra at 200 K in Table 2 and Table S1, we gain insight into the orientation of  $[C_1C_1Im][Tf_2N]$  on the Cu(111) surface at this

temperature as already done earlier for this IL on Au(111) [64]: An intensity decrease at 80° as compared to 0° for certain IL signals of the two-dimensional WL indicates that the corresponding atoms are close to the metal surface and are attenuated by the atoms above, yielding lower than the nominal atom numbers. On the other hand, enhanced signals at 80° indicate that these atoms are near the vacuum, leading to larger than nominal atom numbers at 80°. At 200 K,  $F_{\text{an,sum}}$  exhibits a larger than nominal atom number and  $O_{\text{an,sum}}$  a lower than nominal atom number, indicating that the anion is adsorbed with the oxygen atoms towards the copper surface, while the  $\text{CF}_3$  groups preferentially point toward the vacuum, as it is often observed for ILs of this kind [36]. The cation signals  $C_{\text{cat,sum}}$  and  $N_{\text{cat,sum}}$  are systematically attenuated in 80° indicating that the imidazolium ring is closer to the surface than the  $\text{CF}_3$  groups of the anion. Overall, the adsorption behavior at 200 K thus shows clear similarities to that of comparable ILs on Ag(111) and Au(111) [36, 63, 64]. We therefore conclude also from the XPS data that  $[\text{C}_1\text{C}_1\text{Im}][\text{Tf}_2\text{N}]$  exhibits the checkerboard arrangement at 200 K as it is frequently observed for ILs, in which the anion and cation adsorb alternately next to each other on the surface [36].

We next address the spectra at higher temperatures. At 275 K, new peaks start to appear (marked in red, with an additional asterisk), at the expense of the original peaks (see Figs. 3 and S6), which decrease in intensity. The new peaks all exhibit pronounced shifts towards lower binding energies relative to the peaks of the intact IL at 200 K (see Table S2 in the SI). The anion-related peaks are shifted by  $-2.1$  eV for  $\text{N}_{\text{an}}^*$ ,  $-1.3$  eV for  $\text{O}_{\text{an}}^*$ ,  $-1.1$  eV for  $\text{C}_{\text{an}}^*$ ,  $-0.7$  eV for  $\text{F}_{\text{an}}^*$  and  $-2.0$  eV for  $\text{S}_{\text{an}}^*$ , and the cation-related peaks by  $-1.0$  eV for  $\text{N}_{\text{cat}}^*$  and  $-0.6$  eV for  $\text{C}_{\text{cat}}^*$ . As already mentioned above, in the quantitative analysis in Tables 2 and S1, only the sum of the shifted (\*) and the pristine signals of the IL is given (as indicated with subscript “sum”), in order to provide the total amount for each element.

Upon deposition at 300 K and measuring immediately afterwards, a further increase of the shifted signals and decrease of the unshifted signals is observed in Fig. 3 for 0.5 ML (and in Figure S7 on larger scale), and in Figure S6 for 0.3 ML. This “signal conversion” is even more pronounced when keeping the sample for one day at 300 K after deposition (without X-ray exposure to avoid any beam damage in the meantime), and measuring afterwards. Notably, despite the changes observed for the 275, 300 and 300 K (1 day) spectra, the overall IL composition in 0° (sum of shifted and unshifted signals) is still in good agreement with the nominal values for both investigated coverages (cf. Tables 2 and S1). Thus, no significant loss of individual atoms by desorption occurs up to 300 K (minor deviations might be due to the bad signal-to-noise ratio or indicate changes in ion orientation). The analysis of the XP spectra data for the 0.5 ML film measured immediately after deposition at 300 K in Fig. 3

shows that  $39 \pm 15\%$  of the original anion peaks at 200 K are converted to the new  $\text{N}_{\text{an}}^*$ ,  $\text{O}_{\text{an}}^*$ ,  $\text{C}_{\text{an}}^*$ ,  $\text{F}_{\text{an}}^*$  and  $\text{S}_{\text{an}}^*$  peaks. For the cation peaks, only a much smaller fraction of  $10 \pm 2\%$  is converted to  $\text{N}_{\text{cat}}^*$  and  $\text{C}_{\text{cat}}^*$ . After 1 day at 300 K, the total coverage slightly decreased, and the degree of conversion increases to  $58 \pm 10\%$  of the anions and  $20 \pm 2\%$  of the cations (with the total anion and cation signals still agreeing with the nominal composition; see Table 2). Note that for the 0.3 ML deposition series (see Figure S6), overall the same trend is observed as for the 0.5 ML discussed here, with the conversion to the (\*) species being, however, more pronounced. Most likely, the apparently more reactive situation in case of the 0.3 ML is related to increased beam damage effects since longer measurement times are required at the lower coverage regime to obtain reasonable signals. As will be discussed in detail in the next section, we propose that the unshifted anion and cation signals are due to intact ion pairs on the surface, forming the well-ordered striped phase at 200 K and the hexagonal and honeycomb phases at 300 K. On the other hand, the shifted signals are related to species within the disordered small islands, where cations and anions have partially reacted/decomposed at the copper surface into non-volatile fragments. The smaller fraction of shifted cation signals (as compared to the larger amount of shifted anion signals) is possibly related to the fact that some of the cation fragments still exhibit binding energy values close to the original peaks in contrast to the anion ones (see next section for more details).

At 360 K, the pristine IL signals have virtually disappeared, and only the shifted signals are left (Figs. 3 and S6). In particular, the total amount of  $C_{\text{an,sum}}$ ,  $O_{\text{an,sum}}$ ,  $F_{\text{an,sum}}$  and  $S_{\text{an,sum}}$ , that is, all elements involved in the anion, is reduced to  $\sim 50\%$  compared to the starting point (see Tables 2 and S1). The halving of the anion signals between 300 and 360 K is a strong indication for the desorption of anions or fragments of anions. Notably, this is in line with the in situ temperature-programmed XPS (TPXPS) experiment in Fig. 4 (see below), which also shows a drop of  $\sim 50\%$  starting from 300 K in the  $F_{\text{an}}$  signal (as representative for the whole anion). Simultaneously to the decrease of the total anion intensity, we observe the total conversion of the remaining cation signals  $C_{\text{cat}}$  and  $N_{\text{cat}}$  to the  $C_{\text{cat}}^*$  and  $N_{\text{cat}}^*$  species (at lower binding energies by  $-0.6$  and  $-1.0$  eV, respectively) along with a small intensity decrease, indicating that also the cation coverage is affected by the ongoing surface processes. Note that this situation at 360 K is likely to represent the one at 350 K in Fig. 1d, where only small disordered islands are observed in nc-AFM (for the initial coverage of 0.15 ML). At 500 K, all anion-derived signals have completely vanished (not shown), and only residual carbon and nitrogen species (with an approximate atomic ratio  $C_{\text{res}}: N_{\text{res}} = 5: 1$ ) remain at the copper surface. Moreover, an additional S 2p duplet

at 162.4/161.6 is observed at 500 K, which is attributed to atomic sulphur as a remaining decomposition product.

To follow the thermal evolution of the wetting layer more closely, we deposited 0.5 ML of  $[\text{C}_1\text{C}_1\text{Im}][\text{Tf}_2\text{N}]$  on Cu(111) at 88 K and subsequently heated to 600 K with a linear heating ramp of 2 K/min while performing temperature-programmed (TP)-XPS at normal emission. To minimize beam damage, we restricted our analysis to three core levels: Along with the Cu 2p substrate signal (to follow the overall film thickness), we measured only C 1 s and F 1 s spectra. After the ramp was finished, we recorded an additional data set after flashing to 800 K to look for further changes. Figure 4 depicts the quantitative analysis of the Cu 2p substrate signals, the total F 1 s signals  $F_{\text{an,sum}} (=F_{\text{an}} + F_{\text{an}}^*)$ , and the C 1 s signals of the anion carbon  $C_{\text{an,sum}} (=C_{\text{an}} + C_{\text{an}}^*)$  and cation carbon  $C_{\text{cat,tot}}$  (note that due to the reduced signal-to-noise ratio in this TPXPS series, a clear discrimination of  $C_{\text{cat}}$ ,  $C_{\text{cat}}^*$  and at higher temperatures residual carbon was impossible and we thus provide only the total amount using one broad peak for fitting this binding energy range); carbon intensities have been multiplied by factor four for better visualisation. All signals show characteristic intensity changes with temperature, which are in line with the data in Fig. 3. The  $F_{\text{an,sum}}$  signal stays constant from 100 to  $\sim 300$  K at  $\sim 28$  kcps. At higher temperatures, it decreases by about 50% to reach a plateau at  $\sim 13$  kcps at around 400 K, and finally drops zero at around 500 K. The  $C_{\text{an,sum}}$  signal shows the same change with temperature, which indicates the loss of  $\text{CF}_3$ -groups in course of the reaction/fragmentation discussed above. Note that the increase of the shifted  $F_{\text{an}}^*$  and  $C_{\text{an}}^*$  signals at the expense of the unshifted signals is also seen in the data of the TPXPS experiment (not shown), similar to the observations in Fig. 3. In contrast to the anion signals, the cation signal  $C_{\text{cat,tot}}$  shows much smaller changes in intensity. It initially remains constant until 300 K at  $\sim 18$  kcps, and thereafter only slightly decreases to  $\sim 15$  kcps at 370 K. After a plateau until 450 K, it finally drops to  $\sim 8$  kcps between  $\sim 460$  and 500 K, and then stays constant till 800 K; note that the remaining residual carbon C 1 s peak at 500 and 800 K is much broader compared to the original  $C_{\text{cat}}$  peak.

### 4.3 Comparison of nc-AFM/STM and XPS Results

When comparing the nc-AFM images in Fig. 1 and the XPS data in Figs. 3 and S6, we can derive information on the nature of the different surface species at the different temperatures. At 200 K, the adsorbed IL is found in long-range ordered islands, and the very small, disordered islands are absent in nc-AFM. In this temperature range, XPS only detects species with binding energies characteristic of the intact IL. XPS thus corroborates our interpretation of the microscopy data that at this temperature, namely that the deposited IL forms ordered islands consisting of intact ion

pairs regularly adsorbed next to each other in the checkerboard arrangement, giving rise to the stripe-like appearance as discussed above. At 300 K, we observe the transformation of the stripe-like island structure first to the hexagonal metastable transition phase and finally to the honeycomb structure. At the same time, we also observe an increasing number of small, disordered islands which coexist with the long-range ordered hexagonal and honeycomb phases. Starting at around 275 K, we also observe pronounced changes in XPS, that is, a partial transformation of the original IL peaks to new chemical shifted (\*) peaks. The observed chemical shifts range between 0.7 and 2.1 eV towards lower binding energies for the anion signals and 0.6–1.0 eV for the cation signals. They indicate a chemical reaction with partial decomposition of the IL on the Cu(111) surface. As the formation of the small disordered islands in nc-AFM is observed in the same temperature region as the formation of the new peaks in XPS, we conclude that the small disordered islands are mainly formed by the products of this ongoing reaction, while the remaining unshifted peaks originate from the intact IL ion pairs within the large and well-ordered islands. The small size of the disordered islands indicates that the decomposed species are to some extent mobile on the surface, which allow them to agglomerate into these islands. Notably up to 300 K, no desorption of reaction products occurs, since the sum of IL- and IL\*-signals does not change within the margin of uncertainty of the experiments. Upon heating to 350 K, in nc-AFM a complete conversion to small disordered islands occurs, which in XPS goes along with a complete disappearance of the unshifted peaks due to conversion to the shifted peaks. In addition,  $\sim 50\%$  of the anion signals and 10–20% of the cation signals are lost due to desorption of volatile species.

In the literature, two studies exist on related systems. Biedron et al. performed a detailed comparative XPS, UPS and STM study of  $[\text{C}_8\text{C}_1\text{Im}][\text{Tf}_2\text{N}]$  deposited onto Cu(100) and Au(111) at and above room temperature [46]. They observed that on Au(111), the XPS binding energies of all IL peaks of the layer in direct contact with the surface show only a small uniform shift relative to multilayer spectra. In contrast on Cu(100), they observed that for the first layer, the anion-related signals are shifted to lower binding energy by  $-2.0$  eV for  $\text{N}_{\text{an}}^*$ ,  $-1.5$  eV for  $\text{O}_{\text{an}}^*$ ,  $-0.8$  eV for  $\text{C}_{\text{an}}^*$ ,  $-0.6$  eV for  $\text{F}_{\text{an}}^*$  and  $-1.8$  eV for  $\text{S}_{\text{an}}^*$ , as deduced from their spectra (cf. Figure 6 of [46]; the positions of the cation peaks were difficult to discern); these values agree to within max. 0.3 eV with the values observed for the shifted peaks in this study. At the same time, the stoichiometry corresponded to that of an intact IL. Biedron et al. attributed these shifts to a much stronger interaction of the intact IL with the Cu(100) surface, which they also used to explain the more stable imaging conditions at the monolayer coverages on Cu(100) as compared to Au(111).

The second study was performed by Uhl et al. who deposited 1-butyl-1-methylpyrrolidinium bis(trifluoromethylsulfonyl)imide ([BMP][Tf<sub>2</sub>N]) on Cu(111) at 80 K in the sub-monolayer range, also using STM and XPS for characterization [47]. While up to 200 K no changes were observed, annealing to 300–350 K yielded pronounced shifts of the anion peaks towards lower binding energy by  $-1.1$  eV for C<sup>\*<sub>an</sub></sup>,  $-0.5$  eV for F<sup>\*<sub>an</sub></sup> and  $-2.3$  eV for S<sup>\*<sub>an</sub></sup>, a decrease of oxygen by 60%, and in addition the formation of atomic sulphur, indicating major structural changes of the IL layer and partial decomposition of the anion at this temperature. The binding energies of the shifted anion signals are similar to those found in this study (deviations between 0.1 and 0.3 eV) and also for [C<sub>8</sub>C<sub>1</sub>Im][Tf<sub>2</sub>N] on Cu(100) by Biedron et al. Interestingly, Uhl et al. report essentially unaffected [BMP]<sup>+</sup>-related signals at 300 K, which agrees with the dominance of the unshifted [C<sub>1</sub>C<sub>1</sub>Im]<sup>+</sup> XPS signals of our study at 300 K as shown in Fig. 3: slightly depending on annealing time and initial coverage, only 10–20% of the pristine cation signals are converted at this temperature, in contrast to the much stronger conversion of anion signals.

Based on our results, we are now able to derive a comprehensive understanding of the two studies by Biedron et al. and Uhl et al. and resolve apparent discrepancies [46, 47]. We propose that for all three investigated systems, that is, [C<sub>8</sub>C<sub>1</sub>Im][Tf<sub>2</sub>N] on Cu(100), [BMP][Tf<sub>2</sub>N] on Cu(111), and [C<sub>1</sub>C<sub>1</sub>Im][Tf<sub>2</sub>N] on Cu(111) overall the same adsorption and reaction behavior is observed, with some differences in the reaction temperatures: For adsorption at low temperatures (< 200 K), the corresponding IL adsorbs intact and with signatures typically observed for non-reactive surfaces like Au or Ag, in terms of XPS binding energies and formation of a checkerboard structure. Upon heating to or adsorption at room temperature, a very similar behavior is observed in XPS for the three systems studied that is, the [Tf<sub>2</sub>N]<sup>-</sup> signals exhibit pronounced shifts toward lower binding energies, indicating that for all systems a similar conversion of mainly the anion peaks occurs. In this first step, the cation signals are not (or only moderately) affected. Based on our findings and in contrast to what was proposed by Biedron et al., we assign the observed shifts of the anion peaks not to an enhanced interaction of the pristine IL with the Cu surface, but to a temperature-induced reaction, which progresses with time at 300 K. Above room temperature, in a second step most of the cation signals also show a pronounced shift, while the shifted anion signals remain at the same binding energy, but decrease by 50%. This behavior indicates decomposition of the ILs and/or partial desorption of the ILs or reaction products. After this step, no long-range order can be detected in nc-AFM or STM.

At this point, we have to address the chemical nature of the reaction products formed above 275 K in our sub-ML

studies of [C<sub>1</sub>C<sub>1</sub>Im][Tf<sub>2</sub>N] films on Cu(111). We attribute the simultaneous formation of the new peaks observed in XPS and of the disordered islands in nc-AFM to a reaction/decomposition of the IL on the surface yielding new surface species. These might be related to one (or to a combination) of the following three explanations:

Explanation (1), which is most favoured by us, is the partial decomposition of the IL above 275 K to small and non-volatile fragments such as NH<sub>x</sub>, SO<sub>x</sub>, fluorocarbon species (CF<sub>3</sub>), carbene-like and/or other species, which remain in the small disordered islands on the surface at 300 K. The fact that the degree of conversion of the unshifted to the shifted peaks in XPS is different for the anion and cations (~40% and 10%, respectively, e.g. for 0.5 ML) could indicate that for the cation several decomposition products with different XPS binding energies are formed, one of which is similar to that of the unshifted peaks of the intact IL. After annealing to 360 K, a part of the anion-related fragments (likely charge neutral) has desorbed, as concluded from the ~50% loss of anion signals.

Another decomposition path could be given by explanation (2), where the [C<sub>1</sub>C<sub>1</sub>Im]<sup>+</sup>-cations of the IL are deprotonated in C2-position and Cu-carbenes are formed, binding to the Cu(111) surface or to copper adatoms. The protons would be transferred to copper and could react with the anions to form neutral H[Tf<sub>2</sub>N], which subsequently desorbs above 350 K. For example, the formation of an organometallic copper dicarbene was observed in STM, XPS and DFT calculations by Jiang et al. [66]: The authors reacted 1,3-Dimethyl-1H-imidazol-3-ium-2-carboxylate with Cu(111), which forms [C<sub>1</sub>C<sub>1</sub>Im\*]Cu[C<sub>1</sub>C<sub>1</sub>Im\*] dimers at the surface after CO<sub>2</sub> elimination ([C<sub>1</sub>C<sub>1</sub>Im\*] is denoted here as the carbene after deprotonation of [C<sub>1</sub>C<sub>1</sub>Im]<sup>+</sup> at position 2). An explanation along these lines can, however, be ruled out, since we observe similar changes in the XP spectra with temperature for the related IL [C<sub>1</sub>C<sub>1</sub>C<sub>1</sub>Im][Tf<sub>2</sub>N] (Figure S8 and Table S3 in the SI), where the most acidic proton of [C<sub>1</sub>C<sub>1</sub>Im]<sup>+</sup> in position 2 is replaced by a methyl group, and thus deprotonation should not occur (or should occur only at considerably higher temperatures). Furthermore, carbene formation also appears to be very unlikely since for [BMP][Tf<sub>2</sub>N] on Cu(111) overall a very similar thermal evolution to that of [C<sub>1</sub>C<sub>1</sub>Im][Tf<sub>2</sub>N] on Cu(111) is found (see discussion above).

Finally, we cannot completely rule out a third explanation (3), namely that upon heating to 275 K and above, parts of the intact IL reorganize without decomposition, e.g. by interaction with Cu adatoms, forming a specific Cu-IL complex. The complexation would have to affect the electronic structure of the still intact IL such that the corresponding IL signals exhibit the observed strong decreases in binding energy. The formed Cu-IL complex could also be an initial step towards carbene formation, initiating also the

decomposition of the IL and the desorption of H[Tf<sub>2</sub>N] at 360 K. We consider this last option, however, as rather unlikely.

#### 4.4 Ordered Structures and DFT Calculations

As final step we aim for a more detailed understanding of the ordered structures based on the nc-AFM images in Fig. 1 through corresponding DFT calculations.

##### 4.4.1 Stripe Structure at 200 K

The stripe structure Fig. 1a (right) and Fig. 5a (left) has a rectangular unit cell ( $\gamma = 90 \pm 3^\circ$ ) with vectors  $\vec{a}$  ( $1.90 \pm 0.08$  nm) and  $\vec{b}$  ( $0.90 \pm 0.05$  nm), yielding a unit cell area of  $\sim 1.71$  nm<sup>2</sup> (see Table 1). This structure is similar to the stripy structure observed for the same IL on Au(111), with a unit cell area of  $\sim 0.74$  nm<sup>2</sup>, and one ion pair per unit cell [43]. If we assume a comparable ion pair density in the wetting layer on both surfaces, this is a strong indication that the unit cell on Cu(111) in Fig. 1 and Fig. 5a (left) contains 2 ion pairs, which yields an ion pair density of 1.17 ion pairs/nm<sup>2</sup>. In Fig. 1 (see above), we tentatively assigned the very bright oval protrusion (red ellipses) and the two less bright protrusions (blue ellipses) to two differently oriented anions, and the dark areas in between (black ellipses) to the two cations.

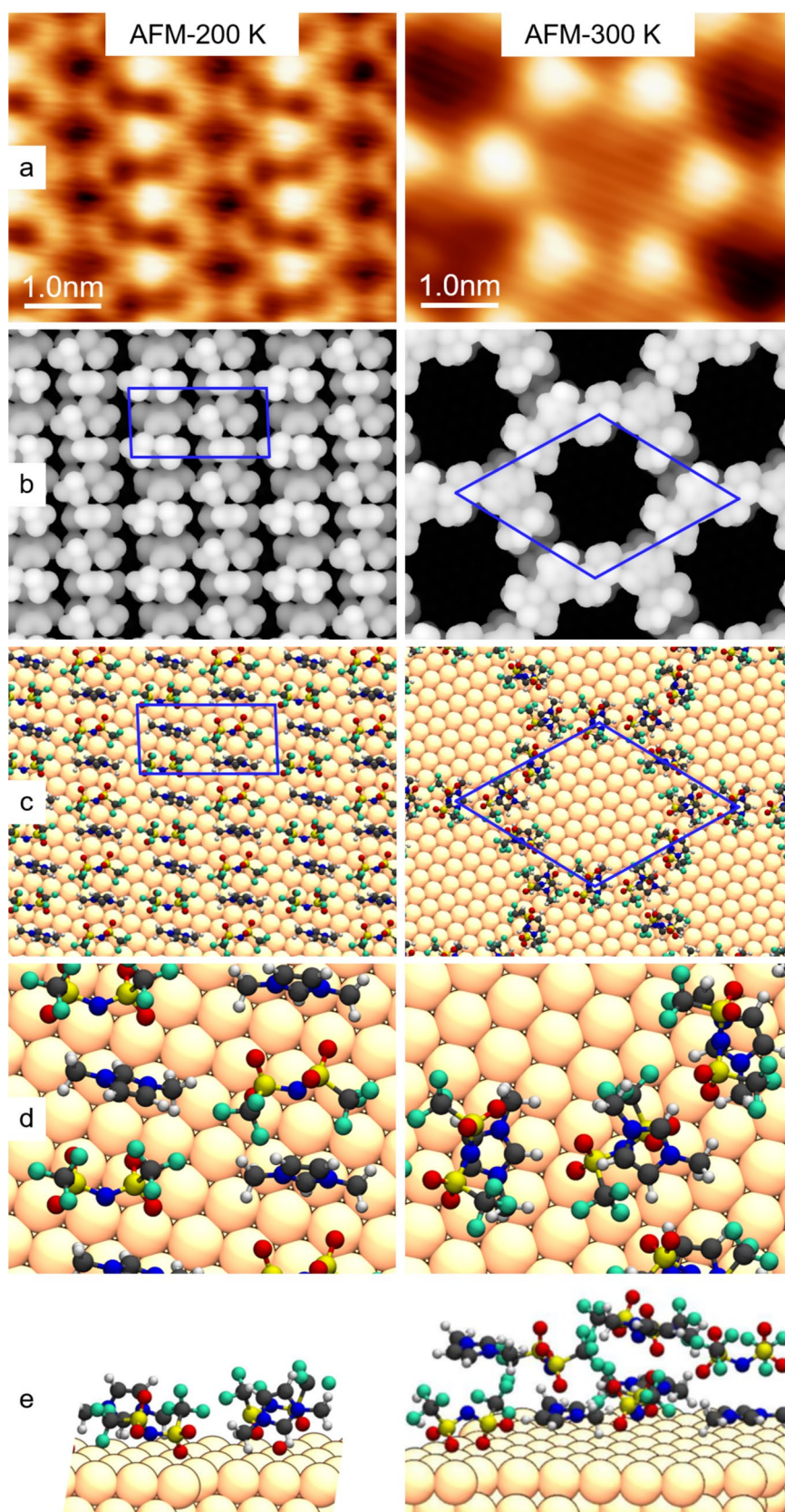
As a next step, we discuss the results from DFT. Because we have a highly ordered structure, we calculated a commensurate structure with a  $\begin{bmatrix} 6 & 2 \\ -3 & 4 \end{bmatrix}$  superstructure. The lattice vectors  $\vec{a}$  (1.83 nm) and  $\vec{b}$  (0.92 nm) with an angle  $\gamma$  of  $92.2^\circ$  yield a unit cell area of  $\sim 1.68$  nm<sup>2</sup>, which (within the margin of error) very well agrees with the experimental values determined from the nc-AFM images. The resulting structure after geometry optimization is shown in Fig. 5c, d and e (left). It reveals two similarly oriented cations with their plane nearly perpendicular to the surface, and the C2 carbon atom of the imidazolium ring pointing downwards, that is, towards the surface. Interestingly, the two anions have different orientations: one is adsorbed nearly vertically with all four oxygen atoms of the sulfonyl groups pointing downwards in 2–2 orientation adsorption motif, and the six F atoms of the two CF<sub>3</sub> groups pointing away from the surface towards vacuum; the other is adsorbed side-on with only one oxygen atom of each sulfonyl group attached to the surface, that is, in 1–1 orientation adsorption motif, and 3 F atoms pointing towards vacuum. These two different orientations are likely responsible for the different contrast of the anions observed by nc-AFM. The DFT structure is also in line with the overall orientation derived from XPS (see above). The resulting adsorption energy  $E_{ads}$ , which is the energy difference between the

isolated ion pair in the gas phase and adsorbed in the proposed layer, yields a value of 3.5 eV per ion pair, indicating a very stable structure. One should note here that small modifications to the unit cell yield quite similar results. In an attempt to simulate the nc-AFM images using a simplified approach, we calculated charge density contour plots; the corresponding image is shown in Fig. 5b (left). The agreement with the experimental data is surprisingly good, considering the fact that the contrast strongly depends on the status of the nc-AFM tip and the simplicity of the calculation. One interesting aspect are the different contributions to the calculated total adsorption energy; the detailed analysis shows that the vertical interaction of the ions with the copper surface via their image charges amounts to  $\sim 1.6$  eV, while the lateral Coulomb interaction within the checkerboard wetting layer amounts to  $\sim 2.0$  eV (see Tables S6 and S7 for details on the different contributions to the adsorption energies; the geometries of the different calculated geometries are provided in a separate zip-file).

##### 4.4.2 Honeycomb Structure at 300 K

We next address the honeycomb structure. The lattice vectors  $\vec{a}$  and  $\vec{b}$  have an identical length of  $2.35 \pm 0.08$  nm, yielding an unit cell area of  $4.78$  nm<sup>2</sup>. It can be described by a  $\begin{bmatrix} 8 & 2 \\ -2 & 10 \end{bmatrix}$  superstructure. Based on the significant fraction of unshifted XPS peaks of anions and cations, we attribute the honeycomb structure to intact IL ion pairs. When addressing the number of ion pairs per unit cell, we have to consider the specific properties of the honeycomb lattice. The unit cell of the honeycomb structure in Fig. 1c (right) and Fig. 5a (right) has 2 bright protrusions (indicated as circles) and 3 dimmer ones (dots). If we assume that the bright protrusions are either anion or cation (and not anions and cations that coincidentally exhibit the same brightness), this immediately implies that the bright protrusions cannot be anions and the dimmer ones cations (or vice versa), as this would violate charge neutrality. One solution is that the bright and dim protrusions are oppositely oriented “sandwiches” composed of stacked cations and anions. Based on our assignment of the well-ordered honeycomb-structure to intact IL ion pairs with unshifted XPS peaks (see previous sections), we propose that the XPS binding energies are not affected by the opposite orientation of the sandwiches; we thus observe only one narrow peak for each element. This structure contains 5 ion pairs per unit cell, which yields an ion pair density of  $1.05$  ion pairs/nm<sup>2</sup>, which is slightly smaller than that of the stripe structure. The fact that some of the pores of the honeycomb structure are empty and some have a dim background is attributed to leftovers of the transformation process.

**Fig. 5** Surface structure of  $[C_1C_1Im][Tf_2N]$  on Cu(111) for the stripe phase (left) and the honeycomb phase (right). **a** nc-AFM images (data from Fig. 1). **b** Charge density plots of the corresponding structures, as derived from DFT calculations. **c** Geometry-optimized structures, as obtained from the DFT calculations. **d** Close-up of the structures shown in (c). **e** Side view of the structures shown in (c). Graphs (a) to (c) are shown on the same scale, as indicated by the scale bars in (a)



For the honeycomb structure with oppositely oriented sandwiches we also performed DFT calculations. The corresponding structure is shown in Fig. 5c, d and e (right) and the corresponding calculated charge density contour plots in Fig. 5b (right). The structure yields an adsorption energy  $E_{ads}$  per ion pair of 3.1 eV, which demonstrates the stability of this porous arrangement. Notably, this adsorption energy value is smaller than the value of 3.5 eV calculated for the nearly rectangular checkerboard-type structure (see above). The reason for the higher adsorption energy of the checkerboard structure is its larger dispersion energy compared to the honeycomb structure; see SI, Table S6. The lower dispersion energy of the honeycomb structure is not surprising because it consists of IL pairs in a sandwich geometry. The top IL molecules of each pair have a larger distance from the metal substrate leading to a smaller dispersion interaction with the substrate. In the checkerboard structure, on the other hand, all IL molecules are in direct contact with the metal substrate structure. One should note that the lower adsorption energy of the honeycomb structure is not expected from the experimental findings, as from a simple consideration one would assume a higher adsorption energy, since upon annealing a transformation towards a more stable structure should occur. Possible reasons are that in the experiment the decomposition of a fraction of the IL layer (yielding the disordered islands) goes along with the formation of the honeycomb structure, and the related energies would have to be included in the total energy balance. An alternative explanation would be that in the calculations, the geometry optimization did not find the global minimum with maximum binding energy. One possible, though unlikely, alternative could be that we actually do not have the structure proposed above, but that a metastable intermediate complex including Cu substrate or adatoms is formed. In particular nitrogen atoms, which are present in the anion and the cation, are known to play an important role in the formation of Cu coordinated frameworks on surfaces [67, 68–70]. The latter considerations are, however, pure speculation.

## 5 Summary and Conclusions

We investigated the initial formation and thermal stability of sub-monolayer ionic liquid films on Cu(111) as a function of temperature with non-contact atomic force and scanning tunneling microscopy, angle-resolved X-ray photoelectron spectroscopy, and density-functional theory calculations. The IL  $[C_1C_1Im][Tf_2N]$  was deposited either at room temperature followed by very fast cooling to 110 K, or directly at low temperatures. Both procedures lead to the adsorption of intact IL on the surface. The thermal evolution of the adsorbate structure and chemical composition was then

investigated by stepwise annealing. The nc-AFM and the STM studies were performed for a coverage of 0.15 ML, which corresponds to ~30% of the surface being covered with a wetting layer of anions and cations adsorbed next to each other in direct contact with the Cu(111) surface. Due to the low signals, the corresponding XPS studies were performed for coverages of 0.5 and 0.3 ML, which correspond to 100% and 60% of the full wetting layer, respectively.

Annealing to 200 K leads to the formation of large islands. Each island consists of one or more domains of a highly ordered phase characterized by molecular rows, that is, stripes with a nearly rectangular unit cell ( $\gamma = 90 \pm 3^\circ$ ), with lattice vectors of  $\vec{a}$  ( $1.90 \pm 0.08$  nm) and  $\vec{b}$  ( $0.90 \pm 0.05$  nm), and a unit cell area of  $1.71$  nm<sup>2</sup>. The checkerboard-type adlayer can be described by a  $\begin{bmatrix} 6 & 2 \\ -3 & 4 \end{bmatrix}$  superstructure; the protrusions visible in nc-AFM are assigned to two types of differently oriented anions and the dark spots in-between to the cations. The chemical composition measured by XPS confirms that at 200 K intact anions and cations are indeed adsorbed next to each other. Based on the nc-AFM and XPS results and the DFT calculations, we propose that the unit cell contains 2 ion pairs, yielding a density of  $1.17$  ion pairs/nm<sup>2</sup>. From DFT, we derived an adsorption energy per ion pair of 3.5 eV, which can be decomposed into a contribution of ~1.6 eV from the interaction with the substrate and ~2.0 eV due to lateral interactions within the IL (see SI, Table S7).

Upon heating to 300 K and annealing at this temperature for hours, we observe a sequence of structural changes in the nc-AFM images which are accompanied by pronounced changes in the XP spectra. In nc-AFM, we observe for the large islands first the transformation of the stripe structure to an overall hexagonal structure and finally to a well-ordered honeycomb-type structure with a pore size of ~2 nm, which goes along with the additional appearance of numerous small disordered islands. Simultaneously, a partial conversion of the initial IL peaks towards peaks shifted to lower binding energies is observed in XPS, which is most pronounced for the anions. From the simultaneous appearance of the small disordered islands and the pronounced changes in XPS, we propose that a chemical reaction yielding partial IL decomposition occurs around 300 K, with the reaction products forming the disordered islands. The large islands with the hexagonal and the honeycomb structure still consist of intact ion pairs. Upon further heating to 350 K, only small disordered islands are observed by nc-AFM, and in XPS, the conversion of all anion and cation signals indicates a complete decomposition of the IL on the surface. Notably at this temperature, nearly 50% of the anion-derived reaction products but only 10–20% of the cationic ones left the surface as deduced from the related signal decreases in XPS.

Interestingly, the well-ordered hexagonal and honeycomb structures of the large islands at 300 K have the identical unit cells with lattice vector lengths  $2.35 \pm 0.08$  nm and a unit cell area of  $\sim 4.78$  nm<sup>2</sup>; they can be described by a  $\begin{bmatrix} 8 & 2 \\ -2 & 10 \end{bmatrix}$  superstructure with an angle of 60°. For the overall hexagonal structure, we assume six ion pairs per unit cell, which yields a density of 1.26 ion pairs/nm<sup>2</sup>, and for the honeycomb structure five ion pairs per unit cell, which yields a density of 1.05 ion pairs/nm<sup>2</sup>. Notably, the honeycomb structure can be obtained from the overall hexagonal structure by removing one ion pair, which results in the pore of the honeycomb structure. Thus, the hexagonal structure can be seen as metastable transition structure from the stripe phase to the honeycomb phase upon annealing the IL layer at 300 K. From the unit cell area and the number of ion pairs per unit cell, we conclude that in the two structures the IL is not adsorbed in the commonly observed checkerboard arrangement with anions and cation next to each other. We rather propose that they adopt a stacked “sandwich structure” of anions and cations, with the sandwiches adsorbed on the surface alternatingly with opposite orientations. Our DFT calculations indeed show that such a structure is quite stable on the surface with an adsorption energy of 3.1 eV.

To conclude, by a combination of experimental and theoretical methods, we were able to obtain detailed insights into the adsorption and reaction of the IL [C<sub>1</sub>C<sub>1</sub>Im][Tf<sub>2</sub>N] on the Cu(111) surface. In contrast to the adsorption of the same IL on Au(111), a very complex thermal evolution with structural changes and decomposition effects was observed even at room temperature due to the more reactive copper atoms. Moreover, our results allowed for solving apparently conflicting results of two previous studies of related ILs on copper surfaces. We are confident that such model thin film studies under well-defined conditions to gain a molecular understanding into IL-metal interactions at interfaces eventually will allow for a more controlled design and use of ILs for particular applications in many areas.

**Supplementary Information** The online version contains supplementary material available at <https://doi.org/10.1007/s11244-023-01801-y>.

**Acknowledgements** Funded by the Deutsche Forschungsgemeinschaft (DFG, German Research Foundation)—Project-ID 431791331 – SFB 1452 (Catalysis at Liquids Interfaces, CLINT).

**Funding** Open Access funding enabled and organized by Projekt DEAL. Funding was provided by Deutsche Forschungsgemeinschaft (Project-ID 431791331).

## Declarations

**Conflict of interest** The authors declare no competing interest.

**Open Access** This article is licensed under a Creative Commons Attribution 4.0 International License, which permits use, sharing,

adaptation, distribution and reproduction in any medium or format, as long as you give appropriate credit to the original author(s) and the source, provide a link to the Creative Commons licence, and indicate if changes were made. The images or other third party material in this article are included in the article's Creative Commons licence, unless indicated otherwise in a credit line to the material. If material is not included in the article's Creative Commons licence and your intended use is not permitted by statutory regulation or exceeds the permitted use, you will need to obtain permission directly from the copyright holder. To view a copy of this licence, visit <http://creativecommons.org/licenses/by/4.0/>.

## References

1. Welton T (1999) Room-temperature ionic liquids. Solvents for synthesis and catalysis. *Chem Rev* 99(8):2071–2084
2. Wasserscheid P, Keim W (2000) Ionic liquids—new “solutions” for transition metal catalysis. *Angew Chem Int Ed* 39(21):3772–3789
3. Wasserscheid P, Welton T (2008) Ionic liquids in synthesis, vol 1. Wiley, New York
4. Plechkova NV, Seddon KR (2008) Applications of ionic liquids in the chemical industry. *Chem Soc Rev* 37(1):123–150
5. Welton T (2018) Ionic liquids: a brief history. *Biophys Rev* 10(3):691–706
6. Binnemans K (2005) Ionic liquid crystals. *Chem Rev* 105(11):4148–4204
7. Crosthwaite JM, Muldoon MJ, Dixon JK, Anderson JL, Brennecke JF (2005) Phase transition and decomposition temperatures, heat capacities and viscosities of pyridinium ionic liquids. *J Chem Thermodyn* 37(6):559–568
8. Piper SL, Kar M, MacFarlane DR, Matuszek K, Pringle JM (2022) Ionic liquids for renewable thermal energy storage—a perspective. *Green Chem* 24(1):102–117
9. Endres F, El Abedin SZ (2006) Air and water stable ionic liquids in physical chemistry. *Phys Chem Chem Phys* 8(18):2101–2116
10. Riisager A, Fehrmann R, Flicker S, van Hal R, Haumann M, Wasserscheid P (2005) Very stable and highly regioselective supported ionic-liquid-phase (SILP) catalysis: continuous-flow fixed-bed hydroformylation of propene. *Angew Chem Int Ed* 44(5):815–819
11. Steinrück H-P, Wasserscheid P (2015) Ionic liquids in catalysis. *Catal Lett* 145(1):380–397
12. Pinilla C, Del Pópolo MG, Lynden-Bell RM, Kohanoff J (2005) Structure and dynamics of a confined ionic liquid. Topics of relevance to dye-sensitized solar cells. *J Phys Chem B* 109(38):17922–17927
13. Zhou F, Liang Y, Liu W (2009) Ionic liquid lubricants: designed chemistry for engineering applications. *Chem Soc Rev* 38(9):2590–2599
14. Cooper PK, Staddon J, Zhang S, Aman ZM, Atkin R, Li H (2019) Nano- and macroscale study of the lubrication of titania using pure and diluted ionic liquids. *Front Chem* 7:287
15. Bresme F, Kornyshev AA, Perkin S, Urbakh M (2022) Electrotunable friction with ionic liquid lubricants. *Nat Mater* 21(8):848–858
16. Avid A, Ochoa JL, Huang Y, Liu Y, Atanassov P, Zenyuk IV (2022) Revealing the role of ionic liquids in promoting fuel cell catalysts reactivity and durability. *Nat Commun* 13(1):1–13
17. Li R, Zhao Y, Chen Y, Liu Z, Han B, Li Z, Wang J (2018) Imidazolate ionic liquids for high-capacity capture and reliable storage of iodine. *Commun Chem* 1(1):1–8



18. Tanner EE (2022) Ionic liquids charge ahead. *Nat Chem* 14(7):842–842
19. Borra EF, Seddiki O, Angel R, Eisenstein D, Hickson P, Seddon KR, Worden SP (2007) Deposition of metal films on an ionic liquid as a basis for a lunar telescope. *nature* 447 (7147):979–981
20. Seddon KR (2003) A taste of the future. *Nat Mater* 2(6):363–365
21. Crowhurst L, Lancaster NL, Pérez Arlandis JM, Welton T (2004) Manipulating solute nucleophilicity with room temperature ionic liquids. *J Am Chem Soc* 126(37):11549–11555
22. Mehnert CP, Cook RA, Dispenziere NC, Afeworki M (2002) Supported ionic liquid catalysis—a new concept for homogeneous hydroformylation catalysis. *J Am Chem Soc* 124(44):12932–12933
23. Riisager A, Fehrmann R, Haumann M, Wasserscheid P (2006) Supported ionic liquids: versatile reaction and separation media. *Top Catal* 40(1):91–102
24. Werner S, Szesni N, Kaiser M, Haumann M, Wasserscheid P (2012) A scalable preparation method for SILP and SCILL ionic liquid thin-film materials. *Chem Eng Technol* 35(11):1962–1967
25. Zhang GR, Etzold BJ (2021) Emerging applications of solid catalysts with ionic liquid layer concept in electrocatalysis. *Adv Func Mater* 31(28):2010977
26. Kalb RS (2020) Toward industrialization of ionic liquids. In: *Commercial applications of ionic liquids*. Springer, New York, pp 261–282
27. Marinkovic JM, Riisager A, Franke R, Wasserscheid P, Haumann M (2018) Fifteen years of supported ionic liquid phase-catalyzed hydroformylation: material and process developments. *Ind Eng Chem Res* 58(7):2409–2420
28. Naicker L, Schörner M, Kremitzl D, Friedrich HB, Haumann M, Wasserscheid P (2022) Influencing the product distribution in citral hydrogenation using ionic liquid modified Cu catalysts. *ChemCatChem* 14(19):e202200388
29. Abai M, Atkins MP, Hassan A, Holbrey JD, Kuah Y, Nockemann P, Oliferenko AA, Plechkova NV, Rafeen S, Rahman AA (2015) An ionic liquid process for mercury removal from natural gas. *Dalton Trans* 44(18):8617–8624
30. Szesni N, Hagemeyer A, Grossmann F, Fischer R, Urbancic M, Lugmair C, Sun M, Hou HC, Lowe DM (2013) Catalyst composition for selective hydrogenation with improved characteristics. Google Patents
31. Endres F, Hoeffft O, Borisenko N, Gasparotto LH, Prowald A, Al-Salman R, Carstens T, Atkin R, Bund A, El Abedin SZ (2010) Do solvation layers of ionic liquids influence electrochemical reactions? *Phys Chem Chem Phys* 12(8):1724–1732
32. Endres F, Borisenko N, El Abedin SZ, Hayes R, Atkin R (2012) The interface ionic liquid (s)/electrode (s): in situ STM and AFM measurements. *Faraday Discuss* 154:221–233
33. Santos CS, Baldelli S (2010) Gas–liquid interface of room-temperature ionic liquids. *Chem Soc Rev* 39(6):2136–2145
34. Lahiri A, Borisenko N, Olschewski M, Pulletikurthi G, Endres F (2018) Anomalous electroless deposition of less noble metals on Cu in ionic liquids and its application towards battery electrodes. *Faraday Discuss* 206:339–351
35. Steinrück HP, Libuda J, Wasserscheid P, Cremer T, Kolbeck C, Laurin M, Maier F, Sobota M, Schulz P, Stark M (2011) Surface science and model catalysis with ionic liquid-modified materials. *Adv Mater* 23(22–23):2571–2587
36. Lexow M, Maier F, Steinrück H-P (2020) Ultrathin ionic liquid films on metal surfaces: adsorption, growth, stability and exchange phenomena. *Adv Phys X* 5(1):1761266
37. Lovelock KR, Villar-Garcia IJ, Maier F, Steinrück H-P, Licence P (2010) Photoelectron spectroscopy of ionic liquid-based interfaces. *Chem Rev* 110(9):5158–5190
38. Steinrück H-P (2010) Surface science goes liquid! *Surf Sci* 604(5–6):481–484
39. Steinrück H-P (2012) Recent developments in the study of ionic liquid interfaces using X-ray photoelectron spectroscopy and potential future directions. *Phys Chem Chem Phys* 14(15):5010–5029
40. Buchner F, Forster-Tonigold K, Uhl B, Alwast D, Wagner N, Farkhondeh H, GrossBehm RJr A (2013) Toward the microscopic identification of anions and cations at the ionic liquid|Ag (111) interface: a combined experimental and theoretical investigation. *ACS Nano* 7(9):7773–7784
41. Uhl B, Cremer T, Roos M, Maier F, Steinrück H-P, Behm RJ (2013) At the ionic liquid|metal interface: structure formation and temperature dependent behavior of an ionic liquid adlayer on Au (111). *Phys Chem Chem Phys* 15(40):17295–17302
42. Uhl B, Huang H, Alwast D, Buchner F, Behm RJ (2015) Interaction of ionic liquids with noble metal surfaces: structure formation and stability of [OMIM][TFSA] and [EMIM][TFSA] on Au (111) and Ag (111). *Phys Chem Chem Phys* 17(37):23816–23832
43. Meusel M, Lexow M, Gezmis A, Schötz S, Wagner M, Bayer A, Maier F, Steinrück H-P (2020) Atomic force and scanning tunneling microscopy of ordered ionic liquid wetting layers from 110 K up to room temperature. *ACS Nano* 14(7):9000–9010
44. Meusel M, Lexow M, Gezmis A, Bayer A, Maier F, Steinrück H-P (2020) Growth of multilayers of ionic liquids on Au (111) investigated by atomic force microscopy in ultrahigh vacuum. *Langmuir* 36(45):13670–13681
45. Meusel M, Gezmis A, Jaekel S, Lexow M, Bayer A, Maier F, Steinrück H-P (2021) Time- and temperature-dependent growth behavior of ionic liquids on Au (111) studied by atomic force microscopy in ultrahigh vacuum. *J Phys Chem C* 125(37):20439–20449
46. Biedron AB, Garfunkel EL, Castner EW Jr, Rangan S (2017) Ionic liquid ultrathin films at the surface of Cu (100) and Au (111). *J Chem Phys* 146(5):054704
47. Uhl B, Buchner F, Gabler S, Bozorgchenani M, Behm RJ (2014) Adsorption and reaction of sub-monolayer films of an ionic liquid on Cu (111). *Chem Commun* 50(62):8601–8604
48. Lovelock K, Kolbeck C, Cremer T, Paape N, Schulz P, Wasserscheid P, Maier F, Steinrück H-P (2009) Influence of different substituents on the surface composition of ionic liquids studied using ARXPS. *J Phys Chem B* 113(9):2854–2864
49. Miller SF, Friedrich HB, Holzapfel CW (2012) The effects of SCILL catalyst modification on the competitive hydrogenation of 1-octyne and 1, 7-octadiene versus 1-octene. *ChemCatChem* 4(9):1337–1344
50. Heinze M, Zill J, Matysik J, Einicke W, Gläser R, Stark A (2014) Solid–ionic liquid interfaces: pore filling revisited. *Phys Chem Chem Phys* 16(44):24359–24372
51. Hoffmann V, Pulletikurthi G, Carstens T, Lahiri A, Borodin A, Schammer M, Horstmann B, Latz A, Endres F (2018) Influence of a silver salt on the nanostructure of a Au (111)/ionic liquid interface: an atomic force microscopy study and theoretical concepts. *Phys Chem Chem Phys* 20(7):4760–4771
52. Lexow M, Heller BS, Maier F, Steinrück HP (2018) Anion exchange at the liquid/solid interface of ultrathin ionic liquid films on Ag (111). *ChemPhysChem* 19(22):2978–2984
53. Horcas I, Fernández R, Gómez-Rodríguez J, Colchero J, Gómez-Herrero J, Baro A (2007) WSXM: a software for scanning probe microscopy and a tool for nanotechnology. *Rev Sci Instrum* 78(1):013705
54. Maier F, Gottfried JM, Rossa J, Gerhard D, Schulz PS, Schwieger W, Wasserscheid P, Steinrück HP (2006) Surface enrichment and depletion effects of ions dissolved in an ionic liquid: an X-ray photoelectron spectroscopy study. *Angew Chem Int Ed* 45(46):7778–7780

55. Kresse G, Hafner J (1993) Ab initio molecular dynamics for liquid metals. *Phys Rev B* 47(1):558
56. Kresse G, Furthmüller J (1996) Efficient iterative schemes for ab initio total-energy calculations using a plane-wave basis set. *Phys Rev B* 54(16):11169
57. Kresse G, Furthmüller J (1996) Efficiency of ab-initio total energy calculations for metals and semiconductors using a plane-wave basis set. *Comput Mater Sci* 6(1):15–50
58. Perdew JP, Burke K, Ernzerhof M (1996) Generalized gradient approximation made simple. *Phys Rev Lett* 77(18):3865
59. Kresse G, Joubert D (1999) From ultrasoft pseudopotentials to the projector augmented-wave method. *Phys Rev B* 59(3):1758
60. Grimme S, Antony J, Ehrlich S, Krieg H (2010) A consistent and accurate ab initio parametrization of density functional dispersion correction (DFT-D) for the 94 elements H-Pu. *J Chem Phys* 132(15):154104
61. Methfessel M, Paxton A (1989) High-precision sampling for Brillouin-zone integration in metals. *Phys Rev B* 40(6):3616
62. Monkhorst HJ, Pack JD (1976) Special points for Brillouin-zone integrations. *Phys Rev B* 13(12):5188
63. Lexow M, Talwar T, Heller BS, May B, Bhui RG, Maier F, Steinrück H-P (2018) Time-dependent changes in the growth of ultrathin ionic liquid films on Ag (111). *Phys Chem Chem Phys* 20(18):12929–12938
64. Cremer T, Stark M, Deyko A, Steinrück H-P, Maier F (2011) Liquid/solid interface of ultrathin ionic liquid films: [C1C1Im][Tf2N] and [C8C1Im][Tf2N] on Au (111). *Langmuir* 27(7):3662–3671
65. Rietzler F, May B, Steinrück H-P, Maier F (2016) Switching adsorption and growth behavior of ultrathin [C2C1Im][OTf] films on Au (111) by Pd deposition. *Phys Chem Chem Phys* 18(36):25143–25150
66. Jiang L, Zhang B, Médard G, Seitsonen AP, Haag F, Allegretti F, Reichert J, Kuster B, Barth JV, Papageorgiou AC (2017) N-Heterocyclic carbenes on close-packed coinage metal surfaces: bis-carbene metal adatom bonding scheme of monolayer films on Au. *Ag and Cu Chem Sci* 8(12):8301–8308
67. Klappenberger F, Weber-Bargioni A, Auwärter W, Marschall M, Schiffrin A, Barth J (2008) Temperature dependence of conformation, chemical state, and metal-directed assembly of tetrapyrrolyl-porphyrin on Cu (111). *J Chem Phys* 129(21):214702
68. Fendt LA, Stöhr M, Wintjes N, Enache M, Jung TA, Diederich F (2009) Modification of supramolecular binding motifs induced by substrate registry: formation of self-assembled macrocycles and chain-like patterns. *Chemistry* 15(42):11139–11150
69. Lepper M, Schmitt T, Gurrath M, Raschmann M, Zhang L, Stark M, Hölzel H, Jux N, Meyer B, Schneider MA (2017) Adsorption behavior of a cyano-functionalized porphyrin on Cu (111) and Ag (111): from molecular wires to ordered supramolecular two-dimensional aggregates. *J Phys Chem C* 121(47):26361–26371
70. Adhikari R, Siglreithmaier G, Gurrath M, Meusel M, Kuliga J, Lepper M, Hölzel H, Jux N, Meyer B, Steinrück HP (2020) Formation of highly ordered molecular porous 2D networks from cyano-functionalized porphyrins on Cu (111). *Chemistry* 26(59):13408–13418

**Publisher's Note** Springer Nature remains neutral with regard to jurisdictional claims in published maps and institutional affiliations.